



PCCP

Structures, Proton Transfer and Dissociation of Hydroxylammonium Nitrate (HAN) Revealed by Electrospray Ionization Tandem Mass Spectrometry and Molecular Dynamics Simulations

Journal:	<i>Physical Chemistry Chemical Physics</i>
Manuscript ID	CP-ART-04-2022-001571.R1
Article Type:	Paper
Date Submitted by the Author:	12-May-2022
Complete List of Authors:	Zhou, Wenjing; Queens College of the City University of New York, Chemistry and Biochemistry Liu, Jianbo; Queens College of the City University of New York, Chemistry and Biochemistry Chambreau, Steven; Air Force Research Laboratory, Vaghjiani, Ghanshyam; Air Force Research Laboratory, AFRL/RQRS

SCHOLARONE™
Manuscripts

Structures, Proton Transfer and Dissociation of Hydroxylammonium Nitrate (HAN) Revealed by
Electrospray Ionization Tandem Mass Spectrometry and Molecular Dynamics Simulations

Wenjing Zhou,^{a,b} Jianbo Liu,^{a,b*} Steven D. Chambreau,^c and Ghanshyam L. Vaghjiani^d

^a Department of Chemistry and Biochemistry, Queens College of the City University of New York,
65-30 Kissena Blvd., Queens, New York 11367, USA;

^b PhD Program in Chemistry, the Graduate Center of the City University of New York,
365 5th Ave., New York, New York 10016, USA;

^c Jacobs Technology, Inc., Air Force Research Laboratory, Edwards Air Force Base, California 93524, USA;

^d In-Space Propulsion Branch, Rocket Propulsion Division, Aerospace Systems Directorate, Air Force Research
Laboratory, AFRL/RQRS, Edwards Air Force Base, California 93524, USA

Abstract Hydroxylammonium nitrate (HAN) is a potential propellant candidate for dual-mode propulsion systems that combine chemical and electrospray thrust capabilities for spacecraft applications. However, the electrospray dynamics of HAN is currently not well understood. Capitalizing on electrospray ionization guided-ion beam tandem mass spectrometry and collision-induced dissociation measurements, and augmented by extensive molecular dynamics simulations, this work characterized the structures and reaction dynamics of the species present in the electrosprays of HAN under different conditions, which mimic those possibly occurring in low earth orbit and outer space. While being ionic in nature, the HAN monomer, however, adopts a stable covalent structure $\text{HONH}_2 \cdot \text{HNO}_3$ in the gas phase. Spontaneous proton transfer between the HONH_2 and HNO_3 moieties within the HAN monomer can be induced in the presence of a NO_3^- , a water ligand or a second HAN monomer within 3 – 5 Å or a H^+ within 8 Å, regardless of their collision impact parameters. These facts imply that HAN proton transfer is triggered by a charge and/or a dipole of the collision partner without the need of chemical interaction or physical contact. Moreover, the addition of NO_3^- to HAN leads to the formation of a stable $^- \text{O}_3\text{N} \cdot \text{HONH}_3^+ \cdot \text{NO}_3^-$ anion in negative electrosprays. In contrast, when a proton approaches the $\text{HONH}_2 \cdot \text{HNO}_3$ structure, dissociative reactions occur that lead to the H_2O , NO_2 and HONH_2 fragments (and their cations) but not intact HAN species in positive electrosprays.

*E-mail: jianbo.liu@qc.cuny.edu. Tel: 1-718-997-3271.

1. Introduction

Due to its reduced toxicity and improved performance, hydroxylammonium nitrate (HAN) is of great interest as a greener alternative to the highly toxic hydrazine¹ and as an add-on in ionic liquid (IL)-based monopropellants²⁻⁵ for spacecraft applications. ILs are chosen for electrospray propulsion owing to their inherent ionic nature, low vapor pressure and high electrical conductivities, yielding high specific impulse but only limited thrust.^{2-4,6} Mixing ILs with HAN potentially enhances mission performance on the basis of the resulting dual-mode capability which combines chemical and electrospray propulsions.⁷⁻⁹ For example, a monopropellant consisting of 1-ethyl-3-methylimidazolium ethyl sulfate (EMIM⁺EtSO₄⁻) and HAN was predicted to provide chemical propulsion performance similar to other state-of-the-art monopropellants such as hydrazine, LMP-103 and ASCENT (a.k.a AF-M315E) and stable electrospray performance as well.^{3,7,8,10} In the electrospray thruster, 100% propellant utilization is desired for mission planning. But many factors result in deviations from the theoretical optimum, one of which is related to the nature of ILs. Protic ILs¹¹ such as HAN undergo reversible proton transfer to form neutrals that evaporate into a vacuum rather than produce ions in the spray, effectively making that fraction of the propellant mass unavailable for ion-thrust generation. Understanding such effects as well as inefficiencies in ion production, extraction and acceleration in the electrospray thruster are important for determining propellant utilization-metrics and optimizing thruster design and operation.

Considering that electrospray ionization (ESI) mass spectrometry closely mimics electrospray thrusters in terms of ion emission and injection into a vacuum, ESI mass spectrometry can be utilized to examine and better understand how an electric propulsion system operates, especially the structures, stabilities and the primary and secondary reactions of the species emerging in the electrospray plumes.⁵ There are many works focusing on the ESI mass spectra of energetic ILs.^{2,12-20} Yet the literature is sparse concerning the impact, if any, of HAN on electrospray performance, plumes and efficiencies, and concerning the operation of electrospray thrusters in alternative positive and negative modes as well as the induced spacecraft charging effects.⁴ One related work concerns the ESI mass spectra of a

monopropellant blend of EMIM⁺EtSO₄⁻ and HAN,^{8, 21} in which ionic species originating from the nitrate in HAN were observed in the negative electrospray (such as NO₃⁻ and HNO₃·NO₃⁻), whereas ionic species originating from EMIM⁺EtSO₄⁻ exclusively dominated the positive electrospray. Herein, we examined the ESI mass spectra of pure HAN solutions in both negative and positive ESI modes by using a guided-ion beam tandem mass spectrometer. Corroborated by molecular dynamics simulations and reaction potential energy surface (PES) explorations, we were able to delineate structures and dynamics of HAN species under various experimental conditions.

The remainder of the paper is organized as follows. We briefly describe the main aspects of experimental setup, data analysis and computational methods in Section 2. The electrospray behaviors of HAN species under different conditions are reported in Section 3. In Section 4, we present molecular dynamics simulations and PES calculations. The results are used to not only interpretate and rationalize ion-molecule experimental results but also explore neutral-neutral reactions of the HAN species. Finally, a conclusion for this article is presented in Section 5.

2. Experimental Setup and Computational Methodologies

2.1 Electrospray Ionization Tandem Mass Spectrometric Measurements

Experiments were carried out on a guided-ion beam tandem mass spectrometer built at Queens College, which was described elsewhere.²² In brief, the apparatus consists of an ESI ion source, a radio-frequency (rf) hexapole ion guide, a quadrupole mass filter, an rf octopole ion guide surrounded by a scattering cell, a second quadrupole mass filter and an electron-multiplier ion detector. In this work, the mass spectrometer was operating in either a positive or a negative ion mode by switching the polarity of electrical potentials applied to electrospray and ion optics in the mass spectrometer.

The HAN sample (82% in water) was prepared at the Air Force Research Laboratory (Edwards Air Force Base) and diluted with appropriate solvent mixtures in the experiment. In the negative ion electrospray, 0.01 M of HAN in acetonitrile/water (v : v = 3:1) was sprayed into the ambient atmosphere (flow rate = 0.06 mL·h⁻¹) through an electrospray needle biased at -4.43 kV relative to ground.

Negatively charged droplets were transmitted into the mass spectrometer through a desolvation capillary (heated to 120 °C and biased at -44 V relative to ground), wherein the charged liquid droplets and solvated ions underwent continuous desolvation as they passed through the capillary and converted into gaseous ions in the source chamber. A skimmer of 1.0-mm orifice is located at the end of the source chamber. The skimmer was biased at -18 V relative to ground. The electrical field between the end of the capillary and the skimmer helped remove remaining solvent molecules attached to ions by collision-induced desolvation²³ and prevented large solvent clusters from appearing downstream.^{24, 25} Ions that passed through the skimmer were transported into the hexapole ion guide. The interaction of ions with background gas (at a pressure of 25 mTorr) within the hexapole led to collisional damping and focusing,²⁶⁻²⁸ through which the internal energies of ions were thermalized to 300 K (according to a previous calibration experiment).²²

For measurement of ESI ion compositions, the first quadrupole mass filter in the guided-ion beam tandem mass spectrometer was operated in the rf-only mode (as an ion guide) to transmit all ionic species, and mass scans were performed by the second quadrupole mass filter. For measurement of collision-induced dissociation (CID), ions were then fed into the first quadrupole mass filter for mass selection. The mass-selected primary ions were focused into the octopole ion guide that passes through the 10-cm scattering cell wherein the primary ions underwent CID with Xe gas (Spectral Gases, 99.95%). In addition to providing an ion trapping potential in the radial direction, the octopole was biased with a DC potential. The DC offset was used to control the kinetic energy of primary ions in the laboratory frame (E_{lab}), thereby setting the collision energy (E_{col}) between ions and collision gas in the center-of-mass (CM) frame, that is $E_{\text{col}} = E_{\text{lab}} \times m_{\text{neutral}} / (m_{\text{ion}} + m_{\text{neutral}})$, where m_{neutral} and m_{ion} indicate the masses of collision gas and primary ions, respectively. In the CID experiment, the collision gas pressure was maintained at 0.02 mTorr and measured using a capacitance manometer. Under this condition, most of the primary ions underwent at most single collisions with Xe gas, *i.e.*, the probability of ions having single collisions with Xe was 1.5%, that of double collisions with Xe was 0.02%, and none of the ions had more than double

collisions. As a result, absolute product ion cross section and reaction energy dependence could be determined in a thin-target limit that is analogous to the Beer-Lambert Law.²⁹ Note that, except for collisional thermalization in the hexapole and Xe-induced collisions within the scattering cell, no ion-neutral collisions were expected for reactant ions within the mass spectrometer high-vacuum chambers, as all of which were evacuated to a pressure of $10^{-7} - 10^{-8}$ Torr.

After passing through the scattering cell, the remaining primary ions and the CID product ions drifted to the end of the octopole and were mass analyzed by the second quadrupole and pulse-counted by the electron multiplier. CID product ion cross sections were calculated from the ratios of primary and product ion intensities, the Xe pressure in the scattering cell and the effective cell length. The entire experiment was repeated four times under the same conditions, from which standard deviations were determined for the measurements.

Positive electrospray of HAN (at a concentration of 0.001 – 0.01 M) was measured in a similar manner, using a variety of solvents including methanol/water ($v : v = 3 : 1$), ethanol/water (3 : 1), acetonitrile/water (3 : 1) and pure water. Due to the extremely low ion intensities presented in the positive mode, the ESI voltage was increased up to +3.4 kV (for comparison, the ESI voltage for a typical 0.001 M electrolyte in methanol/water is +2.3 kV or less).²² The pH of the HAN solution was adjusted by adding a trace amount of acid. HCl was chosen as the acidic medium instead of the conventionally used acetic acid so that contaminants in the ESI mass spectra could be minimized. Note that the pH of the ESI solution did not represent the pH in the electrospray droplets, but it controlled ion compositions and concentrations that may be transferred from the solution to the gas phase.

2.2 Determination of Dissociation Threshold Energy

Due to kinetic energy spread and internal energy of the primary ions and Doppler broadening (i.e., thermal velocity) of the collision gas, CID product cross sections rise from zero at collision energies lower than the true dissociation threshold energies (E_0). To determine exact values of E_0 , the E_{col} -dependent product ion cross sections were fitted using a line-of-centers (LOC) model-based function:³⁰⁻³³

$$\sigma(E_{\text{col}}) = \sigma_0 \frac{(E_{\text{col}} + E_{\text{vib}} + E_{\text{rot}} - E_0)^n}{E_{\text{col}}} \quad (1)$$

where σ_0 is an energy-independent scaling factor, E_{vib} and E_{rot} are reactant vibrational and rotational energies, E_0 and E_{col} are as defined above, and n is a fitting parameter which determines the efficiency of translational-to-internal energy transfer ($T \rightarrow E_{\text{internal}}$) in collisions and therefore controls the slope of $\sigma(E_{\text{col}})$. It was assumed that at the energies near E_0 , at least some collisions are completely inelastic so that all of the E_{col} may contribute to overcome E_0 . This assumption was verified in the threshold CID of various ionic species.³²⁻³⁴ The $\sigma(E_{\text{col}})$ was convoluted over the aforementioned experimental energy broadening and kinetic factors. To this end, a Monte Carlo collision simulation program^{35, 36} was used to mimic the experimental conditions: Xe atoms were sampling a Maxwell-Boltzmann translational kinetic energy distribution at 300 K; the primary ion beam had a kinetic energy spread of 0.7 eV in the laboratory frame as determined in the experiment, and the E_{vib} and E_{rot} of the primary ion were sampled at a temperature of 300 K. A total of 100000 single ion-Xe collisions were simulated at each E_{col} . The established distributions of the Xe gas velocity and the ion kinetic energy, E_{vib} and E_{rot} were then fed into the cross-section fitting routine. To account for kinetic shift in near-threshold collisions³⁷ (i.e., excess energy is required to observe detectable dissociation within a certain experimental time frame),³⁸ a Rice-Ramsperger-Kassel-Marcus (RRKM) model³⁹ was included in the fitting to decide whether each dissociation was detectable within the mass spectrometer ion time-of-flight (up to $\sim 500 \mu\text{s}$). A leveling-off function was used in the fitting to allow $\sigma(E_{\text{col}})$ to reach a plateau at high E_{col} . The rising curvature of $\sigma(E_{\text{col}})$ is highly sensitive to E_0 and n , the values of which were adjusted until the convoluted $\sigma(E_{\text{col}})$ matched the experimental data.

2.3 Electronic Structure Calculations and Direct Dynamics Trajectory Simulations

Direct dynamics for HAN approaching NO_3^- , H^+ , another HAN species and water was simulated using the VENUS^{40, 41} code to set up initial trajectory conditions, and the Hessian-based predictor-corrector algorithm⁴² implemented in Gaussian 16⁴³ to integrate trajectories. Trajectories started at the

optimized geometries of the covalent HAN monomer and its collision partner, with an initial separation of 10 or 11 Å between the centers of mass of the randomly oriented reactants. The trajectories were calculated at various impact parameters (b)³¹ ranging from 0.0 which mimics head-on collisions^{44, 45} up to 3.0 Å which is large enough to explore side scattering reaction dynamics.

Reactant E_{vib} and vibrational modes were sampled using quantum Boltzmann probability distributions at 300 K:⁴⁶

$$P(n_i) = \exp\left(-\frac{n_i h \nu_i}{k_B T_{\text{vib}}}\right) \left[1 - \exp\left(-\frac{h \nu_i}{k_B T_{\text{vib}}}\right)\right] \quad (2)$$

where ν_i and n_i are the vibrational frequency and quantum number of the i^{th} mode, respectively; T_{vib} is the vibrational temperature, k_B is the Boltzmann constant and h is the Planck constant. Quasi-classical initial molecular vibrations were simulated by giving individual atoms displacements (from equilibrium geometries) and momenta that are appropriate to initial rovibrational states, with random phases for different modes. Reactant E_{rot} was sampled from a classical Boltzmann distribution at a rotational temperature (T_{rot}) which was set equal to T_{vib} . 0.05 eV was added as relative translational energy (E_T) in the center-of-mass frame. The term of E_T is analogous to the center-of-mass E_{col} in ion-molecule collisions. We used E_T to indicate that this energy is equivalent to the kinetic energy release in the decomposition of an ion-molecule complex, i.e., imagine the trajectory happens in the reverse direction. For the same reason, E_T was set at a low energy in order to improve complex formation in the trajectories.

Trajectories were propagated at a step size of 0.25 amu^{1/2}Bohr (equivalent to 0.6 fs in trajectory time) with the Hessian matrix updated every 5 steps. The propagation step size is small enough to ensure SCF convergence as well as to keep the system energy and momentum conserved. The ω B97XD/6-31+G(d,p) density functional was chosen for the trajectory simulations, as this functional is able to provide a good description of IL reaction dynamics.⁴⁷ A quadratically convergent SCF method was opted in to integrate trajectories (i.e., SCF = XQC)⁴⁸ in case the conventional first-order SCF algorithm failed to converge within the default cycles. Trajectories were terminated at 2 – 3 ps when the trajectory either reached a geometry of stable product or the reactants (in a non-reactive collision) were separated by more than 11

Å. All trajectory simulations were completed on a Linux computing cluster consisting of 20 nodes, each of which is equipped with an Intel Xeon E5-2696 36-core processor. On average, each trajectory took 210 CPU days. gOpenMol⁴⁹ was used for trajectory visualization. Trajectories were analyzed using in-house custom programs written for these purposes.^{47, 50}

3. Experimental Findings

3.1 HAN·NO₃⁻ Formed in Negative Electrosprays

An acetonitrile/water mixture was used as the solvent for negative ESI to eliminate mono-solvated NO₃⁻ in mass spectra (such as NO₃⁻·CH₃OH and NO₃⁻·C₂H₅OH in alcohol solutions), and the addition of acetonitrile was to prevent the corona discharge at the ESI emitter that would otherwise occur in the negative electrospray of aqueous solution.^{51, 52} As shown in Figure 1a, the negative ESI mass spectrum of HAN was dominated by NO₃⁻ and HNO₃·NO₃⁻ (and their hydrated clusters), as previously observed in the anion mass spectra of the EMIM⁺EtSO₄⁻/HAN mixture.^{8, 21} However, a new species that was captured only in the ESI of pure HAN is the anion of *m/z* 158.

To confirm that *m/z* 158 was not from an impurity in the solvent and verify its structure, ions of *m/z* 158 were selected by the first quadrupole mass filter as the primary ions and subjected to CID with Xe gas in the scattering cell, followed by measurement of product ions and energy dependence in the second quadrupole mass filter in the guided-ion beam tandem mass spectrometer. The CID of the *m/z* 158 primary ions produced only NO₃⁻ fragment ions, as demonstrated in the tandem mass spectrum of Figure 1b. Based on the CID result, *m/z* 158 was assigned as a HAN·NO₃⁻ cluster. Note that the formation of doubly charged dimeric species (HAN·NO₃⁻)₂ or other multiply charged nanoclusters⁵³ at *m/z* 158 could be ruled out based on the following considerations: (1) total ion counts would increase in the CID mass spectrum of (HAN·NO₃⁻)₂ or other multiply charged clusters, as one doubly charged dimer generated two singly charged ions, and (2) a pair of complementary product ions from the fission of a doubly charged dimer would be detected in the CID product mass spectrum. None of these were observed in Figure 1b.

Product ion cross sections of HAN·NO₃⁻ were measured over an center-of-mass E_{col} range of 0.05 –

4.5 eV and the result is presented in Figure 1c, wherein error bars were determined on a basis of four sets of measurements. In order to extract the value(s) of dissociation threshold energy, we needed to take into account the Doppler broadening of Xe gas as well as the kinetic energy spread and the internal energy of the primary ion beam. For this purpose, the product ion cross section was fitted using eqn (1). Note that due to the finite width of the ion beam kinetic energy, a fraction of reactant ion beam was backward scattered in the laboratory frame at E_{col} below 0.3 eV, affecting collection efficiencies of reactant and product ions; as a consequence, the cross section slightly rebounded below 0.3 eV. This should be attributed to an experimental artifact. The CID cross section appears to consist of two components, with one dominating at the low E_{col} range and the other starting to emerge at high E_{col} . No satisfactory fit could be obtained with a single $\sigma(E_{\text{col}})$ function. We have therefore fitted the cross section using two sets of $\sigma(E_{\text{col}})$ functions. E_0 and n of each set were adjusted independently to obtain the best fit to the total cross section. As shown by the blue and green solid lines and the best fit E_0 values indicated in Figure 1c: the first channel has $E_0 = 1.6 \pm 0.1$ eV and $n = 2.4$, reaching a plateau at $E_{\text{col}} = 2.6$ eV; while the second channel has $E_0 = 2.4 \pm 0.1$ eV and $n = 2.5$, starting at $E_{\text{col}} = 1.6$ eV and increasing until $E_{\text{col}} = 4.0$ eV. The uncertainty of the E_0 fit was estimated from the range of E_0 values determined using different sets of fitting parameters. Based on the maximum cross sections for the two product channels we determined in the fitting, their product ratio is 4 : 1.

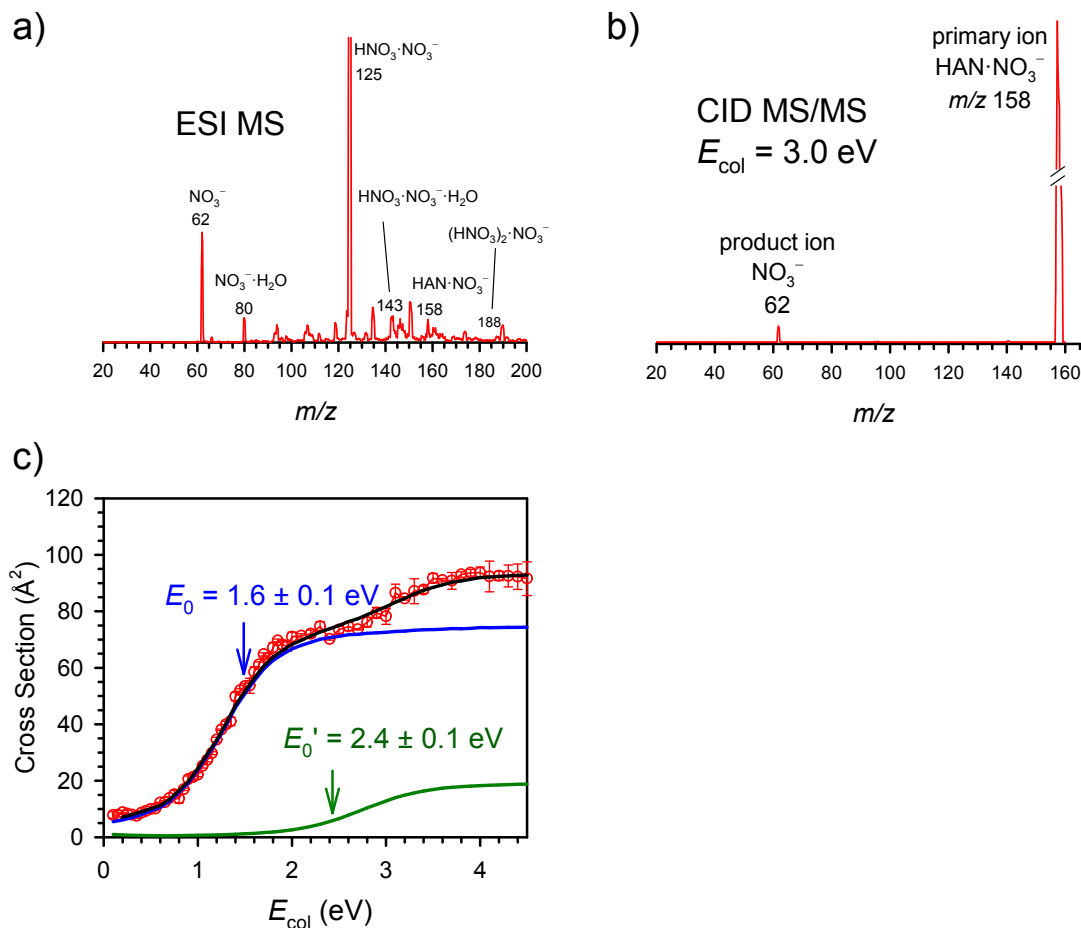


Figure 1 (a) Negative ESI mass spectrum of 0.01 M HAN in 3:1 acetonitrile/water; (b) MS/MS spectrum for the CID product ions of $\text{HAN}\cdot\text{NO}_3^-$ with Xe; and (c) CID product ion cross sections, wherein red circles and error bars are experimental data, the blue and green solid lines represent the LOC fitting for the low- and high-dissociation threshold product channels, and the black solid line represents the sum of the two fits.

3.2 Absence of Intact HAN Species in Positive Electrospays

One issue in the mass spectrometric measurement is that, in contrast to the negative ion electrospay, no intact HAN species was detected in the positive ion electrospay mass spectra. We have attempted to capture HAN species in the positive electrospay of HAN using water, methanol/water, ethanol/water and acetonitrile/water as solvents, and measured mass spectra at pH = 3 and 7, respectively. Note that, the ESI ion intensity of a typical 1 mM cation solution is $\sim 1 \times 10^6$ counts/s measured at an ESI voltage of $\sim +2.3$ kV. On the other hand, a much higher voltage (+3.4 kV) was required to initiate electrospay of HAN solutions, and the maximum ion intensity was only $< 5 \times 10^4$ counts/s. Moreover, all of these mass

spectra are dominated exclusively by protonated solvent clusters and unknown impurities from the HPLC solvents, without the presence of any obvious intact HAN species. Since the positive mass spectra do not indicate the presence of HAN species, the results are provided only in Figure S2 in the Supporting Information so as not to distract from the focus of HAN chemistry here.

4. Trajectory Results and Discussion

4.1 Two Collisionally Activated Complex Structures Formed in HAN + NO₃⁻

To reveal the origin of the two dissociation channels in the CID of HAN·NO₃⁻ (Figure 1), it is necessary to understand the dissociation dynamics of the collisionally activated HAN·NO₃⁻. For this reason, direct dynamics trajectory simulations^{42, 54-56} of HAN·NO₃⁻ were pursued at the ωB97XD/6-31+G(d,p) level of theory. As the experimental CID time scale (10² μs) is many orders of magnitude longer than the practical integration time (up to 10² ps) for quasi-classical direct dynamics trajectories, it would not be possible to observe dissociation products should we calculate the collision trajectories of HAN·NO₃⁻ with Xe near the dissociation threshold energies.

Note that the CID of HAN·NO₃⁻ can be considered to involve two steps: HAN·NO₃⁻ + Xe → HAN·NO₃⁻·Xe (a transient collision complex) $\xrightarrow{-Xe}$ [HAN·NO₃⁻]* (vibrationally excited primary ion), followed by intramolecular vibrational energy redistribution (IVR), and finally, unimolecular dissociation of the activated [HAN·NO₃⁻]*. In view of the large mass and high polarizability of the Xe atom and the relatively long collision time in Xe-induced CID,^{29, 32, 57} the HAN·NO₃⁻·Xe should behave statistically rather than impulsively⁵⁸ and so allows for efficient $T \rightarrow E_{\text{internal}}$ in collisions (as reflected by the value of n in eqn 1). As such, it is the structure of the collisionally activated [HAN·NO₃⁻]* that determines the dissociation mechanism.

Following this idea, we set to calculate the recombination trajectories of the dissociation products HAN + NO₃⁻, wherein the structures of the collisionally activated [HAN·NO₃⁻]* could be reproduced when the trajectories had been propagated sufficiently long to re-form the complexes. Note that, while

the ionic HAN monomer (i.e., $\text{HONH}_3^+\cdot\text{NO}_3^-$) dominates in the solid^{59, 60} and coexists in an equilibrium with a covalent structure (i.e., acid-base pair $\text{HONH}_2\cdot\text{HNO}_3$) in solution,⁸ it converges to a covalent structure in the gas phase,^{8, 60} as verified by a relaxed PES scan along the proton transfer reaction coordinate in an isolated HAN (see Figure S1 in the Supporting Information). This is because the Coulombic stabilization interaction between NH_3OH^+ and NO_3^- is insufficient to compensate for the free energy required for proton transfer.⁶⁰ The trajectories were thus initiated at $\text{HONH}_2\cdot\text{HNO}_3 + \text{NO}_3^-$ with a CM separation of 11 Å and the reactant T_{vib} and T_{rot} of 300 K. E_{T} was set at a low center-of-mass energy of 0.05 eV to mimic near-threshold collisions. As mentioned in the computational section, the trajectory simulations were to follow the reverse reactions of complex dissociation. Therefore, we explored collisions ranging from head-on collisions at small impact parameters to side scattering at large impact parameters (that is within the orientation-averaged hard-sphere collision diameter of 3.5 Å, or, equivalently, the orientation-averaged radius of the resulting complex). We did not explore the collisions with impact parameter up to the Langevin capture diameter⁶¹ (which is 7.5 Å at $E_{\text{col}} = 0.05$ eV), as those collisions initially lead to a reactant-like, weakly bound electrostatic complex rather than a strong ionic or covalent complex, and thus are of less interest.

Four batches of trajectories were completed, each of which contained a total of 100 trajectories and were calculated at an impact parameter of 0.0, 1.0, 2.0 and 3.0 Å, respectively. Indeed, at all impact parameters, most trajectories of $\text{HAN} + \text{NO}_3^-$ were observed to form a long-lived complex that lasted until the end of the trajectory — long enough (more than a ps) for achieving sufficient IVR.⁶² The complex formation probabilities are 82% at $b = 0.0$ Å, 75% at 1.0 Å, 80% at 2.0 Å, and 70% at 3.0 Å. Therefore, there is no dependence of complex-formation probability on the initial impact parameter (b) value, i.e., the opacity function is a constant step function whenever the reactants can get near enough to one another.³¹ It indicates that the reactions are clearly dominated by a complex-mediated mechanism; otherwise, direct scattering would increase at larger impact parameters. The importance of complex formation is that it allows for energy redistribution in collisions in a statistical manner rather than what

would happen in an impulsive direct collision.

A representative trajectory at zero impact parameter is demonstrated in Figure 2. Figure 2a plots the changes in the system potential energy, PE (left axis, where the zero point refers to the sum of reactant electronic energies) and the CM distance (right axis) between the two reactants. The trajectory is initiated from a covalent $\text{HONH}_2\cdot\text{HNO}_3$ and an incoming NO_3^- , as shown in snapshot ①. Oscillations in the PES are due to vibrations in reactants and products, including their zero-point energies (ZPEs). Once the two species approach each other within a CM distance of 5 Å, NO_3^- induces proton transfer in $\text{HONH}_2\cdot\text{HNO}_3$, converting the latter into an ionic structure $\text{HONH}_3^+\cdot\text{NO}_3^-$ as illustrated by snapshot ② at 620 fs. The proton transfer is featured by the variations of reactive bond lengths shown in Figure 2b: breaking the rH-ONO₂ bond and forming a new rHONH₂-H bond at 600 fs and the accompanying charge separation within HAN as demonstrated by the electrostatic potential (ESP)-fitted charge distributions in the reaction system. The NO_3^- -induced proton transfer is accompanied by PE decrease.

${}^-\text{O}_3\text{N}\cdot\text{HONH}_3^+\cdot\text{NO}_3^-$ has a binding energy of 1.55 eV relative to the separated $\text{HONH}_2\cdot\text{HNO}_3$ and NO_3^- . Following the formation of ${}^-\text{O}_3\text{N}\cdot\text{HONH}_3^+\cdot\text{NO}_3^-$, there is a brief proton transfer from HONH_3^+ to the incoming NO_3^- , starting at snapshot ③ in Figure 2c. The $\text{O}_3\text{NH}\cdot\text{HONH}_2\cdot\text{NO}_3^-$ structure is higher in energy than ${}^-\text{O}_3\text{N}\cdot\text{HONH}_3^+\cdot\text{NO}_3^-$ as indicated by the increase in the PE during its formation, and it lasts only ~300 fs before its conversion back to ${}^-\text{O}_3\text{N}\cdot\text{HONH}_3^+\cdot\text{NO}_3^-$ at snapshot ④. The analysis of other trajectories shows that the lifetime of $\text{O}_3\text{NH}\cdot\text{HONH}_2\cdot\text{NO}_3^-$ is no longer than 1000 fs (average ~500 fs) should it form in a trajectory.

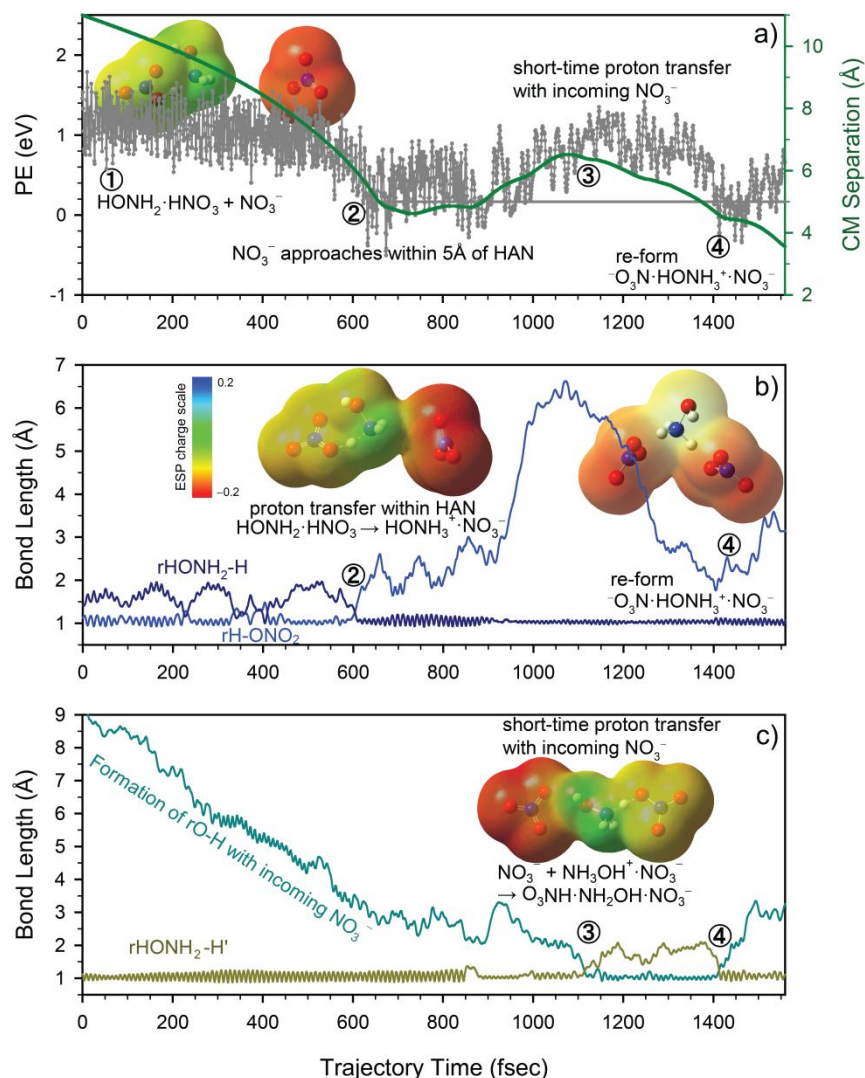
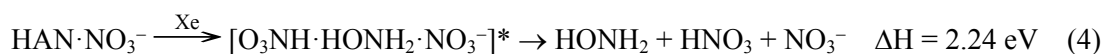
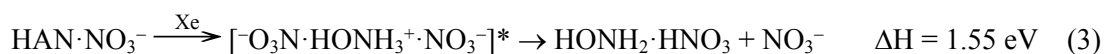


Figure 2 A trajectory for the recombination of $\text{HONH}_2 \cdot \text{HNO}_3$ with NO_3^- at T_{vib} and $T_{\text{rot}} = 300$ K, $E_{\text{T}} = 0.05$ eV and $b = 0.0$ Å, calculated at the $\omega\text{B97XD}/6\text{-}31+\text{G}(\text{d},\text{p})$ level of theory: (a) changes in the system PE (left axis) and CM distance (right axis) between the two reactants, (b) changes of reactive bond lengths, and (c) formation of a short-lived $\text{O}_3\text{NH} \cdot \text{HONH}_2 \cdot \text{NO}_3^-$, followed by its conversion back to ${}^-\text{O}_3\text{N} \cdot \text{HONH}_3^+ \cdot \text{NO}_3^-$. The inset snapshots illustrate the electrostatic potential (ESP)-fitted charge distributions in representative structures along the proton transfer reaction, and the color bar indicates charge scale. Trajectory video is available in the Supporting Information.

We have collected a total of 400 trajectories for $\text{HONH}_2 \cdot \text{HNO}_3 + \text{NO}_3^-$. These trajectories explored various collision orientations and conformations of the neutral HAN⁶⁰ that could be populated at T_{vib} of 300 K. An intriguing finding is that these trajectories, regardless of their randomly selected different

initial conditions and different impact parameters, *all* rearranged to $\text{HONH}_3^+\cdot\text{NO}_3^-$ within the 5 – 6 Å vicinity of the incoming NO_3^- . Despite the fact that there were multiple proton transfer reactions between the HONH_3^+ and one of the two NO_3^- anions in the product ${}^-\text{O}_3\text{N}\cdot\text{HONH}_3^+\cdot\text{NO}_3^-$, 80% of the trajectories eventually converged to ${}^-\text{O}_3\text{N}\cdot\text{HONH}_3^+\cdot\text{NO}_3^-$, and only 20% remained as $\text{O}_3\text{NH}\cdot\text{HONH}_2\cdot\text{NO}_3^-$ at the end of the trajectories. These trajectory results indicate that there are two collisionally activated structures in an equilibrium at high E_{col} , that is $[{}^-\text{O}_3\text{N}\cdot\text{HONH}_3^+\cdot\text{NO}_3^-]^*$ (a major structure) \rightleftharpoons $[\text{O}_3\text{NH}\cdot\text{HONH}_2\cdot\text{NO}_3^-]^*$ (minor, which is not a stable structure in the ground-state PES). Accordingly, there exists two CID channels as follows, for which reaction enthalpies (ΔH) were calculated at the $\omega\text{B97XD}/6\text{-}31\text{+G(d,p)}$ level of theory:



For comparison, reaction enthalpies are 6.10 and 0.68 eV for the dissociation of $\text{HONH}_2\cdot\text{HNO}_3$ to $\text{HONH}_3^+ + \text{NO}_3^-$ and to $\text{HONH}_2 + \text{HNO}_3$, respectively. The product enthalpies of reactions (3) and (4) are in excellent agreement with the E_0 values we determined in the CID experiment of $\text{HAN}\cdot\text{NO}_3^-$ (see Section 3.1). The *b*-weighted average ratio³¹ of $[{}^-\text{O}_3\text{N}\cdot\text{HONH}_3^+\cdot\text{NO}_3^-]^*/[\text{O}_3\text{NH}\cdot\text{HONH}_2\cdot\text{NO}_3^-]^*$ in the trajectories is 4/1, which exactly matches the experimental ratio of the two dissociation channels. Therefore, the trajectory-guided reaction analysis is able to rationalize the CID results in terms of both the dissociation thresholds and the product branching ratio. Note that the $\omega\text{B97XD}/6\text{-}31\text{+G(d,p)}$ -calculated three-body dissociation of $[{}^-\text{O}_3\text{N}\cdot\text{HONH}_3^+\cdot\text{NO}_3^-]^* \rightarrow \text{HONH}_3^+ + 2\text{NO}_3^-$ has a dissociation energy of 7.65 eV. Considering the high dissociation energy, we can safely rule out this pathway in the data analysis.

4.2 Fate of $\text{HAN} + \text{H}^+$

The fact that, despite numerous efforts in optimizing electrospray by manipulating solvent choice, pH, concentration, ESI voltage, flow rate, and inlet capillary temperature, the HAN species were always absent in positive mass spectra (Figure S2) represents a significant finding. This indicates the use of

HAN in electrospray could result in a significant loss of thrust because of neutralization and/or the presence of other reactive channels. To rationalize the lack of HAN species in the positive ESI, we carried out trajectory simulations for H^+ approaching covalent $HONH_2 \cdot HNO_3$. As the idea was to explore the fate of any $[HAN + H]^+$ should it form in the gas phase, a single H^+ was used as the reactant ion despite that the H^+ is attached to a solvent in ionic liquids. Two batches of trajectories (100 trajectories each) were collected at $E_T = 0.05$ eV, T_{vib} and $T_{rot} = 300$ K and with b set at 0.0 and 1.5 Å, respectively.

Surprisingly, unlike the formation of an ionic adduct ${}^{-}O_3N \cdot HONH_3^+ \cdot NO_3^{-}$ in the trajectories of $HONH_2 \cdot HNO_3 + NO_3^{-}$, no protonated $[HAN + H]^+$ was observed in the 200 trajectories acquired for $HONH_2 \cdot HNO_3 + H^+$. Five different primary reaction pathways were identified, which are outlined below. Pathway 1: the H^+ attacked the $-NH_2$ group in the $HONH_2$ moiety to form separated $HONH_3^+ + HNO_3$ (overall trajectory probability = $14 \pm 2\%$). Pathway 2: the H^+ attacked the hydroxy group in $HONH_2$ and formed three-body products $[H_2O + NH_2]^+ + HNO_3$ (probability = $37 \pm 3\%$). Pathway 3: the H^+ collided with and bonded to the HNO_3 side but in the meantime, the ensuing $(HO)_2NO^+$ however transferred its proton to $HONH_2$ (probability = $6 \pm 2\%$), i.e., the HNO_3 acted as a shuttle for proton transfer. Pathway 4: the H^+ attacked the hydroxy group in HNO_3 , followed by quick decomposition of the transient $H_2ONO_2^+$ species to NO_2^+ and H_2O (probability = $12 \pm 2\%$). Pathway 5: proton transfer occurred within the HAN species when the H^+ was approaching within 8 Å of HAN or shorter (probability = $31 \pm 3\%$), and the ensuing NO_3^{-} combined with H^+ to form HNO_3 .

A large fraction of trajectories ($82 \pm 3\%$) proceeded to secondary reactions between primary products, mostly forming three-body products $[H_2O + NO_2 + HONH_2]^+$. A video of a representative trajectory is available in the Supporting Information. The positive charge may be located at any of the three fragments with product formation ΔH of -3.35 eV for $H_2O^+ + NO_2 + HONH_2$, -5.90 eV for $H_2O + NO_2^+ + HONH_2$, and -6.81 eV for $H_2O + NO_2 + HONH_2^+$ (all of the enthalpies were calculated with respect to $HONH_2 \cdot HNO_3 + H^+$).

Indeed, NO_2^+ , $(H_2O)_2^+$ and $HONH_3^+ \cdot H_2O$ clusters, as well as $[HNO_3 + H]^+$ were all detected in the

positive ESI mass spectra (see Figure S2), but not in the case for EMIM⁺EtSO₄⁻/HAN.^{8, 21} The H₂O, NO₂ and HONH₂ products were previously detected in the thermal and catalytic decomposition of HAN.^{59, 63-66} These fragments were also observed in our direct dynamics simulation of HAN at high temperatures (> 1000 K). It can then be concluded that the interaction of HONH₂·HNO₃ with H⁺ breaks the H-bond between the two neutral constituents and leads to catastrophic fragmentation.

4.3 Bimolecular Dynamics of HAN + HAN

Inspired by the contrasting fates of HONH₂·HNO₃ colliding with NO₃⁻ vs. H⁺, a question arose about the dynamics between the neutral HONH₂·HNO₃ species. Trajectories were then calculated for the bimolecular collisions of two HONH₂·HNO₃ monomers at T_{vib} and $T_{\text{rot}} = 300$ K and $E_{\text{T}} = 0.05$ eV. A total of 100 trajectories were calculated at $b = 0.0$ Å, and 50 trajectories each at $b = 1.5$ and 3.0 Å. It is worth noting that, similar to the HAN reactions with NO₃⁻ and H⁺, the bimolecular reaction of HAN does not present notable dependence of product branching ratio on the trajectory impact parameter, indicating that complex-mediated dynamics are dominant in HAN + HAN collisions as well. The reactions could be grouped into three categories. The b -weighted average³¹ probabilities (i.e., opacity functions) for individual product channels are reported below.

1) $19 \pm 3\%$ of the trajectories formed an "ionic" dimer in a *cyclic*-[HONH₃⁺·NO₃⁻·HONH₃⁺·NO₃⁻] structure, as exemplified in Figure 3 and the corresponding trajectory video. The two covalent HONH₂·HNO₃ species start to collide at 1250 fs when their CM distance approaches 5 Å (snapshot ②). One of the covalent HONH₂·HNO₃ species then undergoes intramolecular proton transfer to form an ionic structure HONH₃⁺·NO₃⁻ at 1600 fs (snapshot ③). Almost simultaneously, the other covalent HONH₂·HNO₃ species undergoes a similar proton transfer at 1670 fs (snapshot ④). The product *cyclic*-[HONH₃⁺·NO₃⁻·HONH₃⁺·NO₃⁻] has a binding energy of 0.79 eV with respect to two HONH₂·HNO₃ monomers. This structure is 0.04 eV lower in energy than the previously reported ionic (HAN)₂,⁶⁰ the latter has a C₂ symmetry. Interestingly, when we tried to optimize the single-proton transferred structure

[$\text{HONH}_3^+\cdot\text{NO}_3^- \cdot \text{HONH}_2 \cdot \text{HNO}_3$] formed at snapshot ③ under a static condition without kinetic energy and no internal excitation, the structure converged to the *cyclic*-[$\text{HONH}_3^+\cdot\text{NO}_3^- \cdot \text{HONH}_3^+\cdot\text{NO}_3^-$] form.

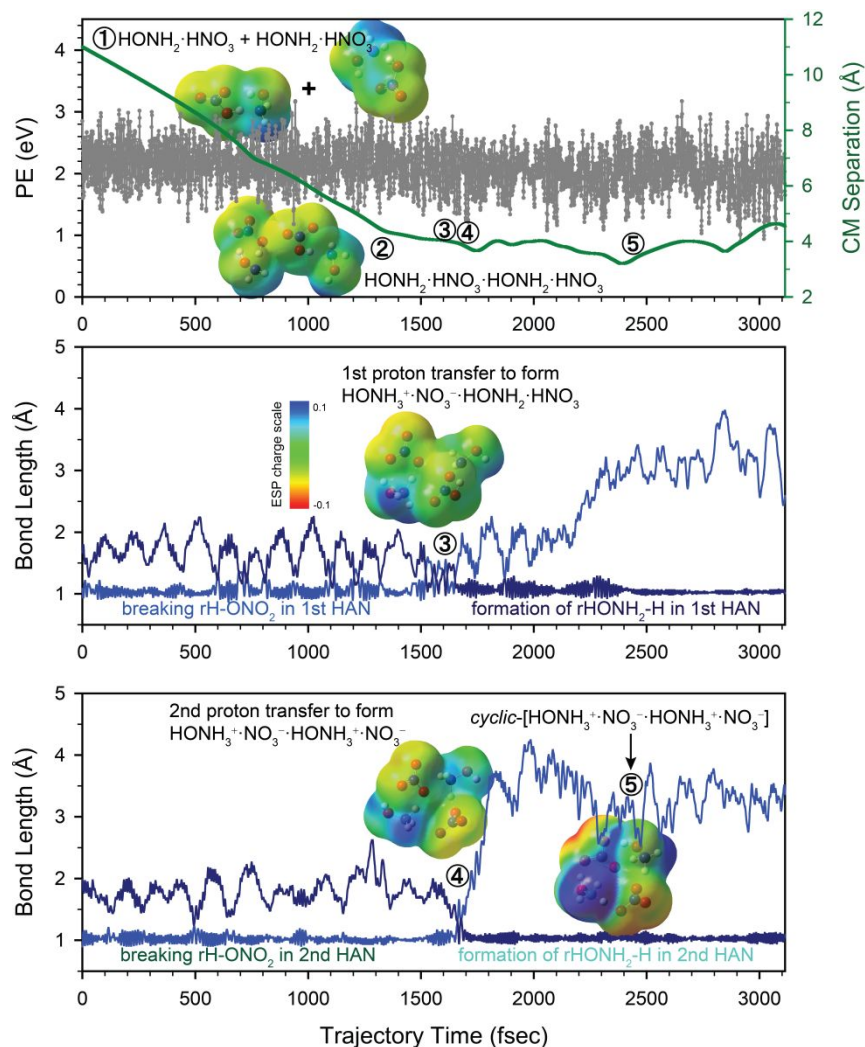


Figure 3 A trajectory for the combination of two $\text{HONH}_2 \cdot \text{HNO}_3$ monomers to *cyclic*-[$\text{HONH}_3^+\cdot\text{NO}_3^- \cdot \text{HONH}_3^+\cdot\text{NO}_3^-$] at T_{vib} and $T_{\text{rot}} = 300$ K, $E_T = 0.05$ eV and $b = 0.0$ Å, calculated at the $\omega\text{B97XD}/6\text{-}31\text{+G(d,p)}$ level of theory: (a) changes in the system PE (left axis) and CM separation (right axis) between the two reactants, (b and c) breaking of rH-ONO₂ bonds in the two HNO₃ moieties and formation of new rHONH₂-H bonds in the two HONH₃⁺ cations. The inset snapshots illustrate the electrostatic potential (ESP)-fitted charge distributions in representative structures along the reaction, and the color bar indicates charge scale. Trajectory video is available in the Supporting Information.

2) $48 \pm 4\%$ of the trajectories led to the formation of covalent (HAN)₂ dimers at the end of the run. An example can be viewed in Figure 4 and the corresponding trajectory video is provided in the Supporting

Information. These covalent dimers are rather floppy, and a large fraction of which may eventually interconvert to the lower energy, more stable ionic dimers through double proton transfer. But some of the covalent $(\text{HAN})_2$ dimers miss an appropriate orientation that is needed to facilitate double proton transfer and therefore remain in the neutral structure, as was also suggested by Alavi *et al.*⁶⁰

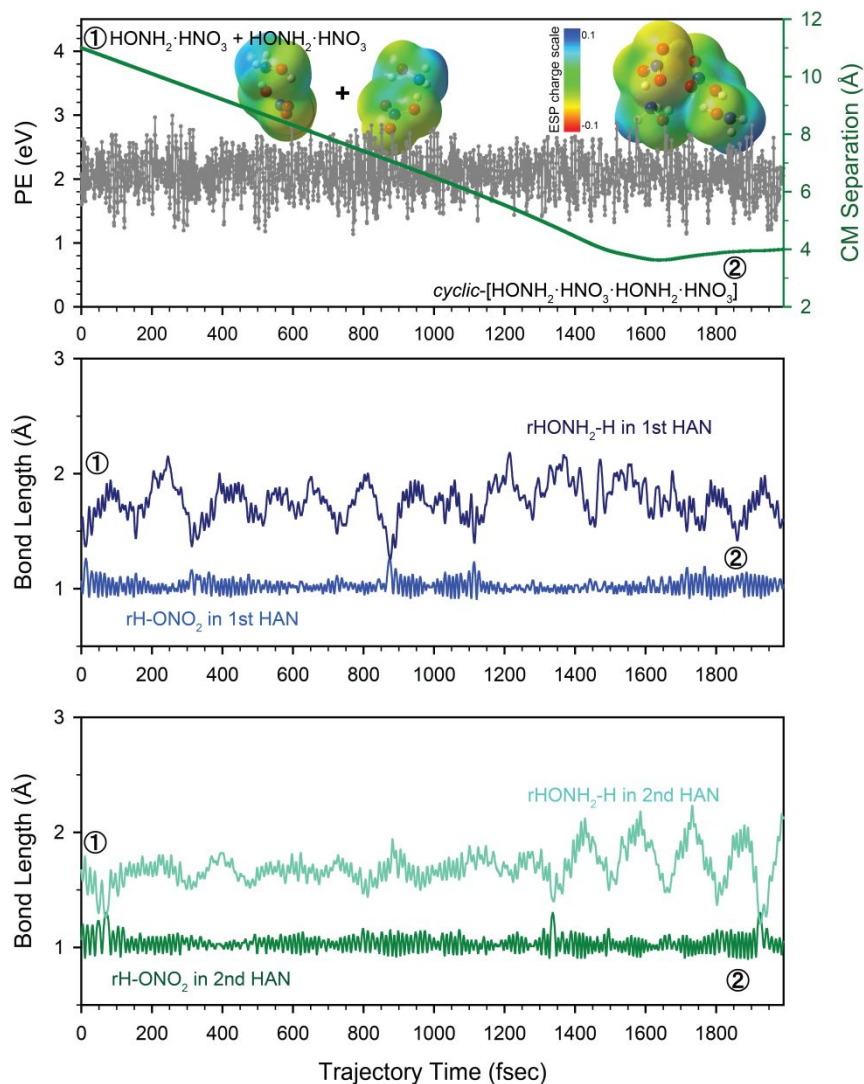


Figure 4 A trajectory for the combination of two $\text{HONH}_2\cdot\text{HNO}_3$ monomers to a covalent dimer at T_{vib} and $T_{\text{rot}} = 300$ K, $E_T = 0.05$ eV and $b = 0.0$ Å, calculated at the $\omega\text{B97XD}/6\text{-}31\text{+G(d,p)}$ level of theory: (a) changes in the system PE (left axis) and CM separation (right axis) between the two reactants, (b and c) changes of rH-ONO_2 bond lengths in the two HNO_3 moieties and $\text{rHONH}_2\text{-H}$ bond lengths with respect to the two HONH_2 moieties. The inset snapshots illustrate the electrostatic potential (ESP)-fitted charge distributions in representative reaction structures, and the color bar indicates charge scale. Trajectory video is available in the Supporting Information.

3) The remaining $34 \pm 3\%$ of the trajectories can be characterized as non-reactive direct collisions, with their encounter times being less than 400 fs.

According to the trajectory simulations, a significant fraction of HAN bimolecular collisions formed an ionic *cyclic*-[HONH₃⁺·NO₃⁻·HONH₃⁺·NO₃⁻]. Figure 5 maps out a 2D PES for the *cyclic*-[HONH₃⁺·NO₃⁻·HONH₃⁺·NO₃⁻] along the reverse proton transfer coordinates from the two HONH₃⁺ to the respective NO₃⁻. The two rH-ONO₂ bond lengths, each of which represents the reaction coordinate for the formation of a HNO₃ molecule, were continuously varied from 1.8 to 0.95 Å at a step size of 0.05 Å. All of the other bond lengths and bond angles were fully optimized at each point. As shown in the figure, the PES for reverse proton transfer is completely uphill. There are no local minima or saddle points that can lead to either single or double reverse proton transfer. The completely repulsive PES reaffirms the *cyclic*-[HONH₃⁺·NO₃⁻·HONH₃⁺·NO₃⁻] structure as a global minimum and reveals a propensity toward ionization in the clusters of protic HAN ionic liquid.

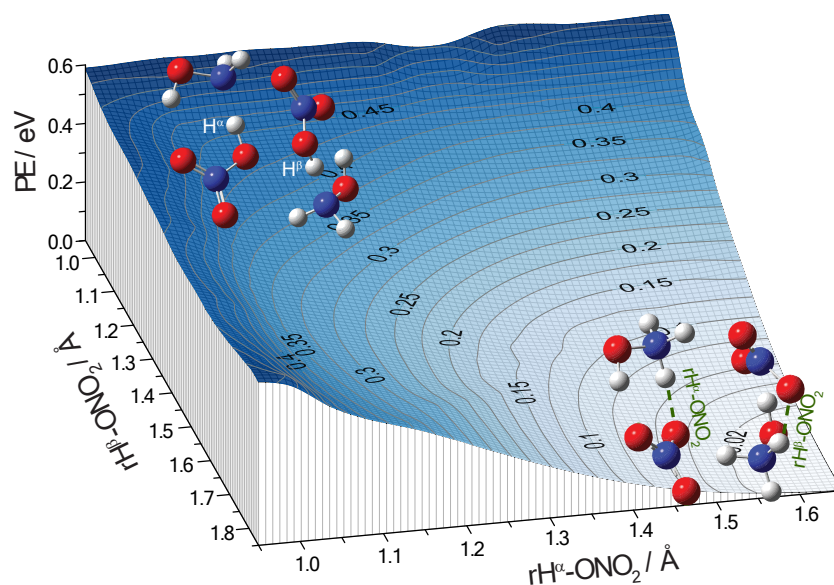


Figure 5 2D PES for reverse proton transfer in *cyclic*-[HONH₃⁺·NO₃⁻·HONH₃⁺·NO₃⁻] calculated at the ω B97XD/6-31+G(d,p) level of theory.

4.4 HAN Proton Transfer Induced by a Water Dipole

Finally, we examined the influence of water on HAN dynamics. Most HAN-based monopropellants

contain more than 10% water.^{1, 67, 68} The addition of water to HAN serves two purposes:²¹ to reduce the combustion temperature, and to enhance the stability of the propellant by building hydrogen bonds within the propellant. The latter in turn presumably inhibits reverse proton transfer in the HAN IL and lowers the HNO₃ concentration in the mixture. However, it is unclear how water affects a single HAN monomer in the gas phase. In this respect, the unimolecular dynamics of HAN upon approach by a water molecule is mapped out using a relaxed 2D PES scan as shown in Figure 6.

In the 2D PES, one scanning coordinate $r_{\text{H-NH}_2\text{OH}}$ describes the proton transfer within the HAN species and the other represents the CM separation between the HAN and water moieties. When their CM separation exceeds 3.2 Å, the HAN species adopts a covalent HONH₂·HNO₃ structure as an isolated HAN in the gas phase (see Figure S1), and the potential energy surface appears to be rather flat (~ -0.1 eV). However, once the water approaches the HAN within a vicinity of 3.2 Å, the system falls into a low-energy valley (-0.35 eV) followed by a spontaneous proton transfer, rolling the structure to a potential energy well (-0.4 eV) corresponding to the ionic HONH₃⁺·NO₃⁻ structure. In this sense, the water provides the HAN species a stabilization energy of 0.3 eV. Interestingly, the amount of this stabilization energy closely matches the sum of a charged-induced-dipole potential energy (-0.10 eV, calculated by $-\alpha q^2/2r^4$ where α denotes the water polarizability, q denotes the ion charge, and r the ion-molecule CM distance)⁶¹ and an orientation-averaged charge-dipole potential energy (-0.21 eV, calculated by $-0.38q\mu_{\text{D}}/r^2$ where μ_{D} is the water dipole moment)⁶¹ at the CM distance of 3.2 Å. It implies that HAN-neutral dipole interaction and charge shift in the HAN species may be developing concomitantly.

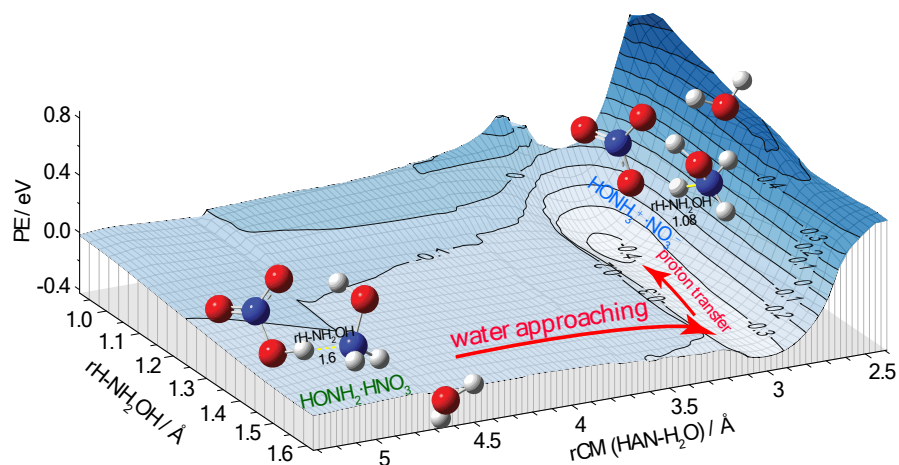


Figure 6 2D PES for water-induced proton transfer in HAN calculated at the ω B97XD/6-31+G(d,p) level of theory.

Even more convincing evidence is provided by the direct dynamics trajectory simulations of a HAN monomer in collision with a water molecule at T_{vib} and T_{tot} of 300 K and E_{T} of 0.05 eV. As can be viewed in a representative trajectory in Figure 7, at the start of the trajectory, the water is separated from the HAN monomer by 10 Å, and the HAN species maintains a covalent structure. The changes of two bond lengths, $r_{\text{H-ONO}_2}$ in HNO_3 and the new $r_{\text{HONH}_2\text{-H}}$ in HONH_3^+ , clearly show that proton transfer happens only during the time when the water is located within 4 Å of the HAN species from, i.e., the highlighted trajectory time leading from snapshot ② to snapshot ③ in Figure 7. Throughout the trajectory, no formation of a hydrogen bond was observed between water and any atoms in HAN. Such results reaffirm that the proton transfer within the HAN species may indeed be induced just by the dipole of a neutral water. Statistically, out of the 100 trajectories we simulated, $42 \pm 5\%$ resulted in water dipole-induced proton transfer in HAN within 4 Å.

This scenario is analogous to what is happening in the collisions of HAN with NO_3^- , H^+ and another HAN, in that the proton transfer occurs in the presence of – but without a direct contact with – the incoming species. Based on these observations, the driving force for the HAN proton transfer should be more appropriately attributed to a long-range ion charge effect and/or a charge-dipole/charge-induced dipole potential.

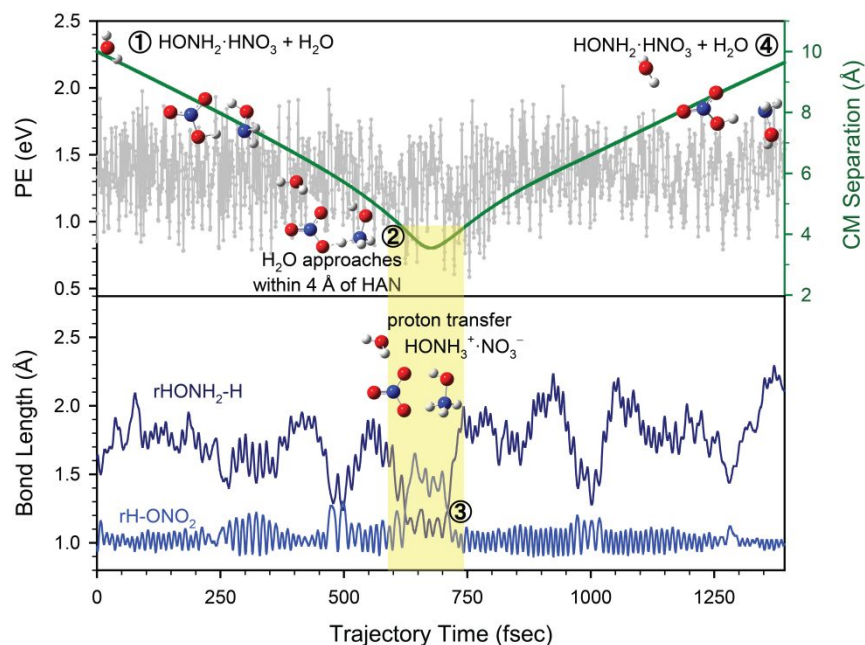


Figure 7 A trajectory for the collision of $\text{HONH}_2 \cdot \text{HNO}_3$ with water at T_{vib} and $T_{\text{rot}} = 300 \text{ K}$, $E_{\text{T}} = 0.05 \text{ eV}$ and $b = 0.0 \text{ \AA}$, calculated at the $\omega\text{B97XD}/6\text{-}31\text{+G(d,p)}$ level of theory: (a) changes in the system PE (left axis) and CM separation (right axis) between the two reactants, and (b) changes of $r\text{H-ONO}_2$ and $r\text{HONH}_2\text{-H}$ bond lengths. Trajectory video is available in the Supporting Information.

5. Conclusions

This work has constituted the first ESI mass spectroscopic study of pure solutions of HAN and molecular dynamics simulations of experimental findings, aimed at exploring what constituents are to be expected in electrosprays and what reactions are likely to happen in the space-environment of electrospray thrusters. A HAN monomer maintains a $\text{HONH}_2 \cdot \text{HNO}_3$ structure in the gas phase, wherein proton transfer can be induced by NO_3^- in negative electrosprays to form ${}^-\text{O}_3\text{N} \cdot \text{HONH}_3^+ \cdot \text{NO}_3^-$, and by another neutral HAN or a water molecule. This work also revealed the dissociative reaction of $\text{HONH}_2 \cdot \text{HNO}_3$ with H^+ and thereby rationalized the lack of intact HAN species in positive electrosprays. Through an understanding of the nature of the ion output of HAN-based electrosprays and the ultimate fate of plume species after ejection into space, the propellant utilization-metric in both positive and negative electrospray modes can be assessed. These results are therefore of importance for modeling spacecraft electrospray thruster performance.

Supporting Information

Cartesian coordinates for the calculated structures, relaxed PES scan along proton transfer in a HAN monomer, positive ESI mass spectra of various HAN solutions, and trajectory videos.

Acknowledgements

J.L. and W.Z. acknowledge Queens College Research Enhancement Award, CUNY Early Research Initiative Catalyst Grant, and the support by the Air Force Research Laboratory through Jacobs Technology Inc. (Subcontract number RAPT1-0000001672). This material is based upon the work supported by the Air Force Office of Scientific Research under award number FA9300-20-F-9801 (S.D.C. and G.L.V.).

References

- 1 R. Amrousse, T. Katsumi, N. Azuma and K. Hori, *Combust. Flame*, 2017, **176**, 334-348.
- 2 B. D. Prince, B. A. Fritz and Y.-H. Chiu, *ACS Symp. Ser.*, 2012, **1117**, 27-49.
- 3 S. P. Berg, J. Rovey, B. Prince, S. Miller and R. Bemish, 51st AIAA/SAE/ASEE Joint Propulsion Conference, Orlando, FL, 2015.
- 4 F. Mier-Hicks and P. C. Lozano, *J. Propul. Power*, 2017, **33**, 456-467.
- 5 A. L. Patrick, *Rapid Commun. Mass Spectrom.*, 2020, **34**, e8587.
- 6 I. Romero-Sanz, R. Bocanegra, J. Fernandez de la Mora and M. Gamero-Castano, *J. Appl. Phys.*, 2003, **94**, 3599-3605.
- 7 S. P. Berg and J. L. Rovey, *J. Propul. Power*, 2013, **29**, 339-351.
- 8 M. J. Wainwright, J. L. Rovey, S. W. Miller, B. D. Prince and S. P. Berg, *J. Propul. Power*, 2019, **35**, 922-929.
- 9 J. Rovey, C. T. Lyne, A. J. Mundahl, N. Rasmont, M. S. Glascock, M. J. Wainwright and S. P. Berg, AIAA Propulsion and Energy 2019 Forum, Indianapolis, IN, 2019.
- 10 S. P. Berg and J. L. Rovey, *J. Propul. Power*, 2013, **29**, 125-135.
- 11 A. Le Donne, S. Russo and E. Bodo, *Chem. Phys.*, 2022, **552**, 111365.
- 12 F. C. Gozzo, L. S. Santos, R. Augusti, C. S. Consorti, J. Dupont and M. N. Eberlin, *Chem. - Eur. J.*, 2004, **10**, 6187-6193.
- 13 P. J. Dyson, I. Khalaila, S. Luetgen, J. S. McIndoe and D. Zhao, *Chem. Commun.*, 2004, 2204-2205.
- 14 G. P. Jackson and D. C. Duckworth, *Chem. Commun.*, 2004, 522-523.
- 15 R. Bini, O. Bortolini, C. Chiappe, D. Pieraccini and T. Siciliano, *J. Phys. Chem. B*, 2007, **111**, 598-604.
- 16 A. M. Fernandes, J. A. P. Coutinho and I. M. Marrucho, *J. Mass Spectrom.*, 2009, **44**, 144-150.
- 17 Y. Fujiwara, N. Saito, H. Nonaka and S. Ichimura, *J. Appl. Phys.*, 2012, **111**, 064901.
- 18 S. W. Miller, B. D. Prince, R. J. Bemish and J. L. Rovey, *J. Propul. Power*, 2014, **30**, 1701-1710.
- 19 D. Krejci, F. Mier-Hicks, R. Thomas, T. Haag and P. Lozano, *J. Spacecraft Rockets*, 2017, **54**, 447-458.
- 20 A. L. Patrick, K. M. Vogelhuber, B. D. Prince and C. J. Annesley, *J. Phys. Chem. A*, 2018, **122**, 1960-1966.
- 21 M. J. Wainwright, J. L. Rovey, S. W. Miller, B. D. Prince and S. P. Berg, AIAA Propulsion and Energy 2018 Forum, Cincinnati, Ohio, 2018.
- 22 Y. Fang and J. Liu, *J. Phys. Chem. A*, 2009, **113**, 11250-11261.

- 23 S. K. Chowdhury, V. Katta and B. T. Chait, *Rapid Commun. Mass Spectrom.*, 1990, **4**, 81-87.
- 24 T. Kim, K. Tang, H. R. Udseth and R. D. Smith, *Anal. Chem.*, 2001, **73**, 4162-4170.
- 25 K. Tang, A. V. Tolmachev, E. Nikolaev, R. Zhang, M. E. Belov, H. R. Udseth and R. D. Smith, *Anal. Chem.*, 2002, **74**, 5431-5437.
- 26 R. M. Moision and P. B. Armentrout, *J. Am. Soc. Mass Spectrom.*, 2007, **18**, 1124-1134.
- 27 A. N. Krutchinsky, I. V. Chernushevich, V. L. Spicer, W. Ens and K. G. Standing, *J. Am. Soc. Mass Spectrom.*, 1998, **9**, 569-579.
- 28 D. J. Douglas and J. B. French, *J. Am. Mass Spectrom.*, 1992, **3**, 398-408.
- 29 P. B. Armentrout, *J. Am. Soc. Mass Spectrom.*, 2002, **13**, 419-434.
- 30 C. Rebick and R. D. Levine, *J. Chem. Phys.*, 1973, **58**, 3942-3952.
- 31 R. D. Levine and R. B. Bernstein, *Molecular Reaction Dynamics and Chemical Reactivity*, Oxford University Press, New York, 1987.
- 32 P. B. Armentrout, *Int. J. Mass Spectrom.*, 2000, **200**, 219-241.
- 33 J. Liu, B. van Devener and S. L. Anderson, *J. Chem. Phys.*, 2002, **116**, 5530-5543.
- 34 M. m. Moe, J. Benny, Y. Sun and J. Liu, *Phys. Chem. Chem. Phys.*, 2021, **23**, 9365-9380.
- 35 M. B. Sowa-Resat, P. A. Hintz and S. L. Anderson, *J. Phys. Chem.*, 1995, **99**, 10736-10741.
- 36 Y. Sun, M. M. Moe and J. Liu, *Phys. Chem. Chem. Phys.*, 2020, **20**, 14875-14888.
- 37 M. T. Rodgers, K. M. Ervin and P. B. Armentrout, *J. Chem. Phys.*, 1997, **106**, 4499-4508.
- 38 C. Lifshitz, *Eur. J. Mass Spectrom.*, 2002, **8**, 85-98.
- 39 R. A. Marcus, *J. Chem. Phys.*, 1952, **20**, 359-364.
- 40 X. Hu, W. L. Hase and T. Pirraglia, *J. Comput. Chem.*, 1991, **12**, 1014-1024.
- 41 W. L. Hase, K. Bolton, P. de Sainte Claire, R. J. Duchovic, X. Hu, A. Komornicki, G. Li, K. Lim, D. Lu, G. H. Peslherbe, K. Song, K. N. Swamy, S. R. Vande Linde, A. Varandas, H. Wang and R. J. Wolf, VENUS 99: A General Chemical Dynamics Computer Program, Texas Tech University Lubbock, TX, 1999.
- 42 V. Bakken, J. M. Millam and H. B. Schlegel, *J. Chem. Phys.*, 1999, **111**, 8773-8777.
- 43 M. J. Frisch, G. W. Trucks, H. B. Schlegel, G. E. Scuseria, M. A. Robb, J. R. Cheeseman, G. Scalmani, V. Barone, G. A. Petersson, H. Nakatsuji, X. Li, M. Caricato, A. V. Marenich, J. Bloino, B. G. Janesko, R. Gomperts, B. Mennucci, H. P. Hratchian, J. V. Ortiz, A. F. Izmaylov, J. L. Sonnenberg, D. Williams-Young, F. Ding, F. Lipparini, F. Egidi, J. Goings, B. Peng, A. Petrone, T. Henderson, D. Ranasinghe, V. G. Zakrzewski, J. Gao, N. Rega, G. Zheng, W. Liang, M. Hada, M. Ehara, K. Toyota, R. Fukuda, J. Hasegawa, M. Ishida, T. Nakajima, Y. Honda, O. Kitao, H. Nakai, T. Vreven, K. Throssell, J. A. Montgomery Jr., J. E. Peralta, F. Ogliaro, M. J. Bearpark, J. J. Heyd, E. N. Brothers, K. N. Kudin, V. N. Staroverov, T. A. Keith, R. Kobayashi, J. Normand, K. Raghavachari, A. P. Rendell, J. C. Burant, S. S. Iyengar, J. Tomasi, M. Cossi, J. M. Millam, M. Klene, C. Adamo, R. Cammi, J. W. Ochterski, R. L. Martin, K. Morokuma, O. Farkas, J. B. Foresman and D. J. Fox, Gaussian 16 Rev. B.01, Wallingford, CT, 2016.
- 44 R. Sun, M. R. Siebert, L. Xu, S. D. Chambreau, G. L. Vaghjiani, H. Lischka, J. Liu and W. L. Hase, *J. Phys. Chem. A*, 2014, **118**, 2228-2236.
- 45 J. Liu, *Phys. Chem. Chem. Phys.*, 2017, **19**, 30616-30626.
- 46 G. H. Peslherbe, H. Wang and W. L. Hase, *Adv. Chem. Phys.*, 1999, **105**, 171-201.
- 47 W. Zhou, J. Liu, S. D. Chambreau and G. L. Vaghjiani, *J. Phys. Chem. B*, 2020, **124**, 11175-11188.
- 48 G. B. Bacskay, *Chem. Phys.*, 1981, **61**, 385-404.
- 49 L. Laaksonen, gOpenMol, Center for Scientific Computing, Espoo, Finland, 3.0 edn., 2005, vol. 3.0, available at www.csc.fi/gopenmol/.
- 50 J. Liu, K. Song, W. L. Hase and S. L. Anderson, *J. Chem. Phys.*, 2003, **119**, 3040-3050.
- 51 M. Yamashita and J. B. Fenn, *J. Phys. Chem.*, 1984, **88**, 4671-4675.
- 52 F. M. Wampler, A. T. Blades and P. Kebarle, *J. Am. Soc. Mass Spectrom.*, 1993, **4**, 289-295.
- 53 D. A. Bonhommeau, R. Spezia and M.-P. Gaigeot, *J. Chem. Phys.*, 2012, **136**, 184503.
- 54 K. K. Baldridge, M. S. Gordon, R. Steckler and D. G. Truhlar, *J. Phys. Chem.*, 1989, **93**, 5107-5119.

- 55 W. L. Hase, *Advances in Classical Trajectory Methods, Vol. 1: Intramolecular and Nonlinear Dynamics*, JAI, Greenwich, Conn., 1992.
- 56 K. Bolton, W. L. Hase and G. H. Peslherbe, in *Modern Methods for Multidimensional Dynamics Computations in Chemistry* ed. D. L. Thompson, World Scientific, Singapore, 1998, pp. 143-189.
- 57 P. B. Armentrout, *J. Anal. At. Spectrom.*, 2004, **19**, 571-580.
- 58 J. Bordas-Nagy and K. R. Jennings, *Int. J. Mass Spectrom. Ion Processes*, 1990, **100**, 105-131.
- 59 J. T. Cronin and T. B. Brill, *J. Phys. Chem.*, 1986, **90**, 178-181.
- 60 S. Alavi and D. L. Thompson, *J. Chem. Phys.*, 2003, **119**, 4274-4282.
- 61 J. Troe, *Chem. Phys. Lett.*, 1985, **122**, 425-430.
- 62 J. Liu and S. L. Anderson, *Int. J. Mass Spectrom.*, 2005, **241**, 173-184.
- 63 D. Amariei, L. Courtheoux, S. Rossignol and C. Kappenstein, *Chem. Eng. Process.*, 2007, **46**, 165-174.
- 64 J. C. Oxley and K. R. Brower, *Proc. SPIE-Int. Soc. Opt. Eng.*, 1988, **872**, 63-70.
- 65 H. Lee and T. A. Litzinger, *Combust. Flame*, 2001, **127**, 2205-2222.
- 66 S. D. Chambreau, D. M. Popolan-Vaida, G. L. Vaghjiani and S. R. Leone, *J. Phys. Chem. Lett.*, 2017, **8**, 2126-2130.
- 67 S. R. Vosen, *Combust. Sci. Technol.*, 1989, **68**, 85-99.
- 68 S. R. Vosen, *Combust. Flame*, 1990, **82**, 376-388.